Co-Ni-B nanocatalyst for efficient hydrogen evolution reaction in wide pH range

S. Gupta[1], N. Patel[1, 2], R. Fernandes[1], R. Kadrekar[1], Alpa Dashora[3], A.K. Yadav[4], D. Bhattacharyya[4], S.N. Jha[4], A. Miotello[2] and D.C. Kothari[1]*

[1]Department of Physics and National Centre for Nanosciences & Nanotechnology, University of Mumbai, Vidyanagari, Santacruz (E), Mumbai 400098, India.

[2]Dipartimento di Fisica, Università degli Studi di Trento, I-38123 Povo (Trento), Italy.

[3]UM-DAE Centre for Excellence in Basic Sciences, Vidyanagari, Santacruz (E), Mumbai 400098, India.

[4]Atomic & Molecular Physics Division, Bhabha Atomic Research Centre, Mumbai – 400 085, India.

* Corresponding Author: **Nainesh Patel,**

Address: University of Mumbai,
Department of Physics,
Vidyanagari, Santacruz (E),
Mumbai 400 098, India
Tel. No.: +91-9967619600
Fax No.: +91-22-26529780
E-mail address: nainesh11@gmail.com

Abstract:

Amorphous Co-Ni-B nanocatalyst with high electrocatalytic activity towards hydrogen evolution reaction (HER) in wide pH range was successfully synthesized. The content of Ni was varied by adjusting the molar ratio Ni/(Ni+Co) in Co-Ni-B from 10% to 50% to identify the most suitable composition for HER. Co-30Ni-B (with 30% Ni) showed the highest catalytic activity and could reach a current density of 10 mA/cm^2 at just 170 mV in pH 7 and 133 mV in pH 14. It also exhibited a Tafel slope value of 51 mV/dec in pH 7 suggesting Volmer-Heyrovsky reaction mechanism for HER. The role of each element in improving the activity was justified with results from XPS, XAS and DFT calculations. It was observed that the presence of Ni promotes higher electron density at Co active sites of Co-Ni-B which in turn facilitates efficient reduction reaction to enhance HER rate. Co-30Ni-B could sustain 1000 cycles and prolonged hours of operation for about 40 hours without losing activity making it an excellent low-cost electrocatalyst material.

Keywords: Hydrogen evolution reaction, Co-Ni-B, wide pH electrocatalyst, amorphous metal borides.

Introduction:

The long foreseen idea of H_2 based economy is now on the verge of becoming a present-day reality owing to the advances in renewable H_2 production techniques involving zero emission. Electrolysis and photo-electrolysis are pivotal methods to produce fuel-cell grade H_2 with no toxic by-product emissions. In either techniques, the role of an electrocatalyst that can facilitate efficient oxidation of H_2O molecules and reduction of protons is of prime importance. Traditionally, Pt and other noble group elements (Pd, Ru, Rh, Ir, etc.) have been frontrunners showing the highest activity and stability in all working environments (acidic, neutral and basic) [1-4]. But, their scarcity and high cost are major drawbacks in their large scale commercialization. It is therefore essential to search for electrocatalysts made up of inexpensive and abundant materials that can imitate the efficiencies of noble group elements and also withstand different pH conditions.

In the past few years, there has been a plethora of earth-abundant electrocatalytic materials for hydrogen evolution with excellent efficiency and stability [5-13]. A lot of recent research is focused on using transition metals (Fe, Co, Ni, Mo, etc.) coupled with non-metals (P, N, C) and chalcogenides (S, Se) such as MoS [5, 6], CoS [7], $CoSe_2$ [8], WSe_2 [9], Mo_2C [10], MoP [11], FeP [12], Co_2P [13] and so on. These metal/non-metal or metal/chalcogenide compounds have turned out to be highly efficient catalysts for hydrogen evolution reaction (HER) with many of them being active in multiple pH environments as well. However, there have been very few reports on transition metal borides as HER active material. About two decades ago, Lasia and Los [14] reported amorphous Ni_2B electrocatalyst for HER in alkaline medium. Subsequently,

there were more reports on electrodeposited Ni_2B [15] and doped Ni_2B [16] catalysts for alkaline water electrolysis. Since then, the interest in metal boride electrocatalysts almost vanished until Vrubel and Hu reported MoB [17] as HER active material in both acidic and basic conditions. In our previous report [18], we presented for the first time, Co-B electrocatalyst as a HER candidate active in wide pH range (4 – 9). Very recently, electroless plated NiBx films [19] were reported to be extremely active in all pH media presenting a strong support to the effectiveness of metal borides for HER.

Herein, we report Co-Ni-B nanocatalysts, prepared by a facile reduction method, to be highly active for HER in various pH media. The reported catalyst turns out to be an excellent alternative to noble electrocatalysts in the sense that it comprises all low-cost, earth-abundant, non-noble and non-toxic elements. Co-Ni-B with Ni/(Ni+Co) molar ratio of 30% (Co-30Ni-B) works exceedingly well under benign neutral conditions with H_2 onset potential of just 53 mV and a Tafel slope of 51 mV/decade. Co-30Ni-B outperforms previously reported Co-B [18] and many other cobalt-based electrocatalysts because of the inclusion of Ni in Co-B leading to a higher electron density at Co active sites thereby facilitating the HER process.

Materials and methods:

Synthesis:

Co-Ni-B catalyst powder was synthesized by reducing aqueous mixture of cobalt chloride [$CoCl_2.6H_2O$] and nickel chloride [$NiCl_2.6H_2O$] in presence of a strong reducing agent like sodium borohydride [$NaBH_4$] which also acts as a boron source, following the method reported by Fernandes et al [20]. The molar ratio of metal to $NaBH_4$ was taken as 1:3 to ensure complete

reduction of Co and Ni ions. $NaBH_4$ being a strong reducing agent causes a highly exothermic reaction turning the aqueous solution black instantaneously with lots of effervescence. Once the effervescence ceases, the final solution was centrifuged to separate the remnant black powder which was further cleaned with DDW and ethanol to remove unwanted ions (Cl- , Na+) and other impurities from the powder formed. The cleaned powder was then vacuum dried at room temperature to obtain the final nanocatalyst. The proportion of Ni in CoNiB was varied by adjusting the molar ratio χ_{Ni}=Ni/(Ni+Co) in the starting aqueous mixture (from 10% to 50%) to identify the most suitable composition (χ_{Ni}=30 %) of Co-Ni-B for electrocatalytic water splitting. For comparative studies, Co-B and Ni-B powders were also synthesized in a similar manner by using only $CoCl_2$ and $NiCl_2$ salts in the initial solution respectively.

Characterization:

Structural characterization of all the catalyst powders was performed by conventional X-Ray Diffractometer (Rigaku Ultima IV) using the Cu K_α radiation (λ = 1.5414 Å) in Bragg-Brentano (θ-2θ) configuration. X-ray photoelectron spectroscopy (XPS) was used to determine the surface electronic states and the related atomic composition of the catalysts. XPS was acquired using a monochromatic Al K_α (1486.6 eV) X-ray source and a hemispherical analyzer using a PHI 5000 Versa Probe II instrument. Appropriate charge compensation was required to perform the XPS analysis and binding energies were referenced to the C 1s peak. Elemental composition of the catalyst powders was determined using X-ray fluorescence (XRF). The BET surface area of the powder catalysts was determined by nitrogen absorption at 77 K (Micromeritics ASAP 2010)

after degassing the powders at a temperature of 423 K for 2 hrs. The surface morphology of the catalyst samples was analyzed by a scanning electron microscope (SEM-FEG, INSPECT F50, FEI). To determine the size of the nanoparticles formed, a transmission electron microscope (TEM) was used (FEI Tecnai G2, F30 TEM microscope operating at an accelerating voltage of 300 kV). HR–TEM image and selected area electron diffraction (SAED) pattern were also recorded. To probe the local structure of Co-B and Co-30Ni-B catalysts, X-ray Absorption Spectroscopy (XAS) studies were done (see details in supporting information).

DFT calculation details:

To understand the charge transfer trend in pure and Ni doped Co-B clusters, we performed density functional theory based calculations using the Dmol^3 code [21] of Material Studio. The crystal structure of Co_2B was built using experimental structural parameter. Co_2B compound accepts a tetragonal cell with space group I4/mcm having cell parameters a = b = 5.015Å and c = 4.220Å. The crystal structure thus built was geometry optimised and using this as a base structure, a 5Å X 5Å X 5Å nanocluster was constructed. DFT formalism was implemented to perform geometry optimisation of the Co_2B nanocluster which displayed random arrangement of Co and B atoms. Charge transfer was studied using the Mulliken charge analysis for pure and Ni doped Co-B clusters of size 5Å X 5Å X 5Å. The PBE gradient corrected functional [22] was used for exchange and correlation and the double numerical plus polarization (DNP) basis set was used. Spin unrestricted calculations were performed in order to obtain accurate results.

Preparation of catalyst modified glassy carbon (GC) electrode:

A 3 mm glassy carbon electrode was polished to remove any form of contaminants from the surface. 5 mg of the catalyst was dispersed in 1 ml ethanol, with 10 µL of 5% Nafion, under continuous sonication, to obtain a homogenous catalyst ink. 30 µL of this ink (in steps of 10 µL) was drop-casted onto the GC surface and dried under ambient environment to obtain a uniform catalyst film with geometric surface area of 0.07 cm^2 and a mass loading of ~2.1 mg/cm^2.

Electrochemical measurement:

$HClO_4$ (0.1 M) and NaOH (1 M) were used as the electrolytes for all the electrochemical measurements at extreme pH values of 1 and 14 respectively. For neutral pH (7), 0.5 M potassium phosphate buffer solution (KPi) was prepared by mixing K_2HPO_4 and KH_2PO_4 in appropriate concentrations. 0.5 M KH_2PO_4 and 0.4 M K_2HPO_4 solutions were used as electrolytes for the measurements at pH = 4.4 and pH = 9.2 respectively. Prior to their use, all the electrolyte solutions were purged with pure N_2 gas for about 20 min to remove dissolved oxygen. All the electrochemical measurements were performed with a potentiostat-galvanostat system (PGSTAT 30) from Autolab equipped with electrochemical impedance spectroscopy (EIS). The electrochemical cell used a conventional three electrode design with catalyst modified GC electrode as the working electrode, a saturated calomel electrode as the reference and a Pt sheet (0.5 cm^2) as the counter electrode. The reference electrode was calibrated with respect to reversible hydrogen electrode (RHE) following a reported method [23]. The calomel electrode was immersed in a cell filled with H_2 saturated electrolyte where one Pt sheet served as the counter while another Pt sheet as the working electrode. CV measurements at a scan rate of 1 mV/s were recorded and average of the two potentials, where current becomes zero,

was considered as the thermodynamic potential for HER. The measured potentials were later converted to RHE by adding a value of 0.241 + (0.05916 x pH). In 0.1 M $HClO_4$, E(RHE) = E(SCE) + 0.301; in 0.5 M KPi, E(RHE) = E(SCE) + 0.655 and in 1 M NaOH, E(RHE) = E(SCE) + 1.068.

The actual polarization measurements were performed at a sweep rate of 5 mV/s under continuous stirring (~ 900 rpm) to avoid accumulation of gas bubbles over the GC electrode. The series resistance (Rs) values were determined using impedance measurement data to compensate for iR losses (Rs = 5 Ω, 3Ω and 1 Ω for pH = 1, 7 and 14 respectively). Tafel slope and exchange current density values were obtained by linear fitting the plot of log (i) versus overpotential (η) in the range of η = 0 - 300 mV. Turnover frequency (TOF) value was determined using a reported procedure [24]. BET technique was used to establish the actual surface area of the Co-30Ni-B catalyst used for the electrochemical measurements. Long-term stability was examined in potentiostatic mode by maintaining the potential at a constant value and measuring the resultant current density for 45 hours. Reusability behavior of the catalyst was tested by conducting cyclic voltametric sweep for 1000 cycles in the range between -0 V and -0.25 V (vs RHE) with a scan rate of 100 mV/s. To verify there was no contamination of the WE by contents of Pt electrode, XPS measurement was done for Co-30Ni-B catalyst after rigorous testings in pH 7.

Results and discussion:

The molar ratio of CoNiB catalyst was confirmed by XRF (table S1). The reduction reaction of metal salts (Co and Ni) by sodium borohydride leads to the formation of well-dispersed spherical nanoparticles of narrow size distribution as observed in SEM image of Co-Ni-B (Fig 1a)

with χ_{Ni}=30 % (Co-30Ni-B). The average size of Co-30Ni-B NPs was determined to be around 27±2 nm, acquired from the TEM image shown in Fig 1b and having a surface area of 16.8 ±0.2 m^2/g obtained by BET analysis. Similar morphology (Fig. S1) and surface area (16.4±0.2 m^2/g) is recorded for Co-B NPs catalyst powder. The vigorous nature of the synthesis reduction reaction doesn't allow the formation of well-ordered structures and thus the resultant NPs are amorphous in nature. The absence of long-range ordering in Co-30Ni-B was confirmed from high resolution TEM micrograph (Fig 1c) which shows no signature of any crystalline phase; the result is also supported by the SAED pattern (inset of 1c) showing diffused rings. XRD pattern (Fig. 1d) of Co-30Ni-B shows a single broad peak centered at $2\theta = 45^o$ confirming the amorphous nature of the catalyst powder formed.

XPS spectra of Co-30Ni-B catalyst (Fig 2 (a-c)) display two peaks in both $Co2p_{3/2}$ and $Ni2p_{3/2}$ levels with binding energies of 774.45 and 780.45 eV for Co, and 852.2 and 855.5 eV for Ni indicating that the two metals are present in both elemental and oxidized states respectively. Apart from the two peaks stated above, an additional shake up satellite peak was also observed at BE of 784.45 eV for Co and 860.63 eV for Ni in $2p_{3/2}$ core level. These characteristic peaks are also present in corresponding $2p_{1/2}$ core levels of both metals. Similarly, two peaks were also observed for B 1s state with BE of 187.6 and 191.5 eV indicating the presence of elemental and oxidized boron respectively. The presence of surface oxidized states in all the samples can be attributed to the exposure of the catalyst samples to ambient atmosphere during the measurements. To make a comparative study, XPS analysis was also carried out for Co-B, Co-50Ni-B and Ni-B catalysts (fig S2). On making a thorough study of the BE peaks obtained by XPS, one observes that in Co-B catalyst, the elemental boron peak (187.8 eV) is positively shifted by

about 0.8 eV as compared to the BE of pure B (187.0 eV), consistent with our previous report [18]. This shift results from an electron transfer from the alloying B to the vacant d-orbital of metallic Co, thus making the B atom electron deficient and the Co atom electron enriched. Since B is more electronegative than Co, this unusual electronic behavior in amorphous Co-B was also confirmed by computational studies in our previous report [18]. A similar phenomenon was also observed in the cases of Co-30Ni-B, Co-50Ni-B and Ni-B catalysts where B 1s peak is again found to be positively shifted (187.6 eV) by 0.6 eV as compared to that of pure B (187.0 eV) indicating an electron transfer from B to vacant d-orbitals of Co (or Ni in Ni-B), correlating well with the trend shown by amorphous metal borides [25, 26]. However, in both the Co-Ni-B catalysts, a negative shift in the BE peak of elemental Co (777.45 eV for Co-30Ni-B and 777.5 eV for Co-50Ni-B) by 0.45 – 0.5 eV was observed which was not detected in Co-B catalyst. This shift in BE indicates the presence of higher electron density on cobalt sites in the cases of both Co-Ni-B(χ_{Ni}=30 % and 50%) catalysts as compared to Co-B. One of the crucial requirements for a good HER catalyst is the presence of high electron density at the catalytically active sites which can facilitate reduction of water molecule more efficiently [27]. From the above XPS results, it is certain that Ni plays a key role in increasing the electron density at Co sites to make them more active for HER. Also, on analyzing the surface composition from XPS data (Table S2), it is revealed that Co-30Ni-B shows boron enrichment on the surface which implies more electrons are available to be transferred from the surface of B atom to Co active sites as compared to Co-B catalyst [20].

X-ray absorption studies (XAS) studies were also carried out to determine more details about the local geometric and electronic structure of the catalysts. The XANES spectra of Co-30Ni-B

and Co-B measured at Co K edge are shown in Fig. 2d along with that of Co metal foil and commercial CoO powder, where Co is present in elemental and +2 oxidation states respectively. The line shapes obtained here for the CoB and Co-30Ni-B samples agree well with that reported by Luo et al [28]. Three points are indicated in the Fig.2d as A, B and C in the edge parts of XANES spectra. In the region B, cobalt oxide shows sharp white line, while Co-B and Co-30Ni-B displayed broad absorption edge like metallic cobalt. Though the XANES spectra of Co-B and Co-30Ni-B samples resemble more that of the Co metal, the features in the regions A and C are quite different which manifests that Co does not exist in pure elemental form in these samples. A linear combination fit of the XANES spectra of the samples with that of pure Co and CoO suggests the presence of Co in metallic as well as in Co^{2+} state in the samples. The feature denoted by A is shifted to slightly lower energy side for Co-30Ni-B compared to that for CoB sample which is due to the excess electron density at Co site in Co-30Ni-B compared to CoB. This correlates well with our XPS observations further supporting our conclusion on the charge transfer on Co.

To investigate it further, we have carried out EXAFS analysis on these samples. Figure 2e and 2f respectively show the normalized FT-EXAFS spectra of Co-B and Co-30Ni-B catalysts measured at Co K edge. The structure and lattice parameters of Co_2B have been used to generate the theoretical FT-EXAFS spectra [29]. The bond distances and disorder (Debye-Waller) factors (σ^2), which give the mean square fluctuations in the distances, have been used as fitting parameters. The best fit results are summarized in Table S3. σ^2 values are found to be very high due to the amorphous nature of the sample as discussed in XRD and HRTEM results. In the case of Co-B, the first peak around 1.9 Å (phase uncorrected spectra) in Fig. 2e has a contribution from first

coordination shell of four B atoms and second coordination shell of six Co atoms at distances of 2.04 Å and 2.48 Å respectively and these bond lengths are consistent with other studies [28,30]. However, the coordination numbers obtained in the present case are quite different from the reported results. The χ(R) versus R plot for the Co-30Ni-B sample is similar to that of Co-B sample where the 1st peak has contributions from first neighboring shell of four B atoms and second neighboring shell of six Co atoms with a slight decrease in bond lengths to 2.02 Å and 2.43 Å, respectively. However, the contributions in the 2nd peak are quite different for Co-B and Co-30Ni-B samples. For Co-B, the second peak in the FT-EXAFS spectra can be fitted by considering only Co-B and Co-Co shells while the doublet in Co-30Ni-B second peak is properly fitted only after taking into account a Co-Ni shell along with Co-Co and Co-B shells. Most importantly, B coordination increases to 10 whereas Co coordination decreases to 3 for the Co-30Ni-B sample as compared to that of Co-B catalyst which has 6 B coordination and 6 Co coordination. This clearly suggests that the inclusion of Ni creates an atomic arrangement where Co is surrounded by higher number of B atoms than that of Co atoms which will contribute to the increased electron density on Co sites by electron transfer from boron. This is in good agreement with XPS results showing boron enrichment.

The results obtained from XPS and XAS studies complement the fact that the addition of Ni in Co-B enhances the electron density on cobalt sites. To corroborate these results, we also performed theoretical calculations using density functional theory (DFT) and found the total charge on each element in Co-B and Co-25Ni-B catalyst. DFT formalism was implemented to perform geometry optimisation of the Co_2B nanocluster which displayed random arrangement of Co and B atoms (Fig S3). From the present calculations, the charge transfer in pure Co-B

nanocluster was estimated from B to Co wherein the average charge on Co was calculated to be -0.0067 e^- and average charge on B atoms was +0.0195 e^-. To check the effect of Ni doping, 25% Ni doping was considered in Co-B cluster at various doping sites (Fig S3). After Ni doping, the average charge obtained on Co atoms was -0.0098 e^- which is higher than that obtained with pure Co-B nanocluster. On the other hand, positive average charge is noted on Ni (+0.0121 e^-) and B (+0.01431 e^-) atoms. Thus, the addition of Ni increases the negative charge on Co atom in Co-25Ni-B cluster which again confirms the results obtained by XPS and XAS analysis.

All the synthesized nanocatalysts were tested for electrocatalytic activity at various pH values by loading them on a polished glassy carbon (GC) electrode. Fig 3a shows the linear polarization curves in neutral media (pH = 7) for Co-Ni-B catalyst with different χ_{Ni} values. As the Ni concentration is increased, the HER improves up to χ_{Ni}= 30% and then decreases. Thus Co-30Ni-B catalyst which showed the optimum HER activity was chosen for further studies. Fig 3b shows the linear polarization curves for Co-30Ni-B, Co-B, Ni-B, Pt and bare GC electrode in pH 7 (0.5 M KPi) potassium phosphate buffer solution at a scan rate of 5 mV/s. The obtained current densities for catalyst modified GC electrodes were normalized to the geometric surface area of bare GC electrode. To achieve the benchmark current density of 10 mA/cm^2 (ideal value for solar fuel synthesis) [31], Ni-B and Co-B require 309 mV (vs RHE) and 203 mV (vs RHE) respectively whereas Co-30Ni-B could achieve the same at just 170 mV (vs RHE). Here, it must be noted that the activity shown by Ni-B powder is much lower than that reported for Ni-Bx films [19] which could be due to different synthesis techniques adopted. The above overpotential values clearly indicate that the ternary alloy Co-30Ni-B yields better HER activity than binary alloys of Co-B and Ni-B which can be attributed to the higher electron density

created at the Co sites of Co-30Ni-B as evident from our findings. However, Pt still remains the best catalyst requiring just 50 mV (vs RHE) of overpotential to reach 10 mA/cm^2 of current density. Co-30Ni-B shows H_2 onset potential value of just 53 mV (vs RHE) (overpotential to achieve 0.5 mA/cm^2) which is extremely competitive with other non-noble electrocatalysts employed in similar neutral conditions (Table S4). Co-30Ni-B could achieve even higher current densities of 20 mA/cm^2 and 40 mA/cm^2 at benign overpotentials of 213 mV and 251 mV respectively. The overpotential values reported here are one of the best results to our knowledge obtained for any metal boride electrocatalysts in pH 7.

The Tafel plot is an important tool in evaluating the performance of an electrocatalyst. It leads us to obtain two crucial electrochemical parameters – Tafel slope (b) and exchange current density (i_0). Tafel slope refers to the overpotential required to raise the current density by one order of magnitude. Fig 3c shows Tafel plots for Co-30Ni-B, Co-B, Ni-B and Pt. For Co-30Ni-B, a Tafel slope of 51mV/dec was obtained which is much lower than that of Co-B (71 mV/dec) and also lower than that reported for the best electrocatalysts operating in neutral conditions such as Co-S film (93 mV/dec) [7], Co-P/CC NWs array (93 mV/dec) [32], FeP/CC (70 mV/dec) [33], $Ni_{0.33}Co_{0.67}S_2$ (67.8 mV/dec) [34], CoS_2 NWs (87.1 mV/dec) [34] and Co-P/Ti (58 mV/dec) [35]. It is well known that the value of Tafel slope is indicative of the reaction steps in HER. The first step is the proton discharge step (Volmer step, 120 mV/dec) followed by electrochemical desorption (Heyrovsky step, 40 mV/dec) or chemical desorption (Tafel step, 30 mV/dec). A value of 51 mV/dec for Co-30Ni-B suggests Volmer-Heyrovsky reaction mechanism [36, 37].

From Tafel analysis, we could also determine the exchange current density (i_0). The exchange current density for Co-30Ni-B in pH 7 was 0.708 mA/cm^2 which again establishes its supremacy over Co-B catalyst (i_0 = 0.501 mA/cm^2). However, Pt shows the highest i_0 value of 1 mA/cm^2. Here, it must be noted that the exchange current density of Co-30Ni-B is only lower than that of $Ni_{0.33}Co_{0.67}S_2$ (0.893 mA/cm^2), NiBx films (0.851 mA/cm^2) and CoS_2 NWs (0.976 mA/cm^2) and is superior to all other non-noble electrocatalysts in pH 7 (Table S4).

The intrinsic activity of each catalytic site can be estimated on the basis of turnover frequency (TOF). Following the method reported by Popczun et al. [37], TOF was determined at different overpotentials in pH 7 using BET surface area (Fig. S4) values. Co-30Ni-B demonstrated a TOF of 0.145 atom^{-1}s^{-1} at an overpotential of 250 mV (vs RHE). This value is underestimated as we have considered all the surface atoms as active which is not true. The real HER activity per active site would be even higher if actual number of active Co sites can be estimated. Even after this underestimation, the TOF value reported here is higher than that of H_2 Co-cat (0.022 atom^{-1}s^{-1} at 385 mV) [38] and Co-S film (0.017 atom^{-1}s^{-1}) [7], all for pH 7 (Table S5).

It is always desirable to obtain an electrocatalyst that can work equally well under different pH conditions. Microbial electrolyzers operate in neutral pH conditions which make them more benign. To be used in an alkaline electrolyzer, the catalyst needs to work efficiently in severe basic conditions whereas PEM electrolyzers demand extreme acidic conditions. All these electrolyzers function on potable water (clean water) which is less than 1 % of the earth's water resources. It would be a big leap if electrolyzers could use water directly from natural resources such as rain and sea (unclean water). To achieve this, we would need electrocatalysts that can

function efficiently in mild acidic conditions of pH 4.2 - 6 relevant to rain water and mild basic conditions of pH 8.1 – 9.5 relevant to sea-water. With these notions in mind, we tested Co-30Ni-B catalyst in different pH media, specifically, 1, 4.4, 7, 9.2 and 14. The corresponding polarization curves are shown in Fig 4a. We observe that Co-30Ni-B works considerably well in different pH conditions and the performance improves as we go to higher pH values. Table S6 quantifies the performance of Co-30Ni-B in various pH media. Fig. 4b shows the variation in overpotential required to achieve a current density of 2 mA/cm^2 in various pH conditions. The overpotential decreases from acidic to basic media with values of 209 mV, 170 mV, 83 mV, 60 mV and 45 mV (all vs RHE) for pH 1, 4.4, 7, 9.2 and 14 respectively signifying that Co-30Ni-B is capable of HER under different pH conditions with most suitable in basic media (Table S6).

Under acidic conditions (pH 1), the overpotentials required to achieve 5 mA/cm^2 and 10 mA/cm^2 of current density were 333 mV and 479 mV (vs RHE) respectively. These values are higher but are still comparable to that of transition metal based HER catalysts including Co-B [18], Mo_2C [39] and MoN/C [40]. On the other hand, in extreme basic conditions (pH 14), Co-30Ni-B could achieve the current densities of 5 and 10 mA/cm^2 at just 93 and 133 mV (vs RHE) respectively and could go up to 100 mA/cm^2 at just 233 mV (vs RHE), as evident from Fig. 3d. These values are higher than that of many non-noble HER catalysts such as Mo_2C [17], MoB [17], CoNx/C [36], Co-NCNTs [41], Co-NPs@N-C [42], MoS2-CPs [43] and Fe2P/NGr [44] working in alkaline conditions. Exchange current density of 0.830 mA/cm^2 and 0.073 mA/cm^2, and Tafel slope of 121 mV/dec and 123 mV/dec was obtained from the Tafel plot (Fig. S6) for Co-30Ni-B catalyst in pH 14 and pH 1 respectively.

The higher HER activity in Co-B is mainly attributed to the electron transfer from boron to d-band of Co [18]. These Co active sites with higher electron density improve the electron donating ability of Co, thereby promoting HER. In Co-Ni-B, the presence of Ni causes boron enrichment on the surface which further activates these Co sites by providing excess electrons as confirmed by XPS, EXAFS, XANES and DFT calculations. This is the main reason of higher HER activity obtained for Co-Ni-B as compared to Co-B having similar morphology and surface area. By electron transfer, boron also protects the Co sites from oxidation and deactivation, thus offering high stability in extreme conditions. Considering the HER rates of Ni-B and Co-B, it seems that Co is more active in borides than Ni. Thus, as the Ni concentration increases, the cobalt sites are further activated by electron density but after χ_{Ni}= 30%, the Co sites are replaced by less active Ni sites causing reduction in HER activity.

To be used on an industrial scale, the electrocatalysts must be able to sustain long hours of operation and reuse. Hence, it becomes essential to test the catalysts for stability and long-term durability. Based on the performance, we chose neutral and alkaline media for these tests. Fig 4c shows polarization curves for Co-30Ni-B catalyst cycled over 1000 times in pH 7 and pH 14. In both the pH conditions, we observe negligible loss in activity even after 1000 cycles of reuse (less than 5% in pH 7 and no loss in pH 14). Co-30Ni-B was also subjected to continuous operation for over 45 hours at constant overpotentials of 110 mV (vs RHE) in pH 7 and 120 mV (vs RHE) in pH 14. From inset of Fig 4d, we see that in neutral pH, the current density falls marginally after 45 hours (maybe due to some atoms detachment from the surface) whereas it remains more or less the same in pH 14 leading to a linear charge build up over time (Fig 4d).

These results illustrate the excellent stability and reusability of Co-30Ni-B catalyst in pH 7 and pH 14 making it ideal for industrial applications.

Conclusion:

By a facile reduction method, we prepared Co-Ni-B powder nanocatalysts which are highly effective for HER in a wide pH range. The content of Ni was varied by tuning the molar ratio Ni/(Ni+Co) in Co-Ni-B from 10% to 50% to identify the most suitable composition (30 %) of Co-Ni-B for HER. High resolution TEM micrograph proved the absence of long-range ordering in Co-30Ni-B while XPS analysis of the Co-Ni-B catalysts showed a negative shift (0.45 eV) in the BE peak of elemental Co which indicates the presence of higher electron density on Co sites as compared to Co-B. By XPS, EXAFS, XANES, and DFT calculations performed on random arrangement of atoms, it was proved that in Co-Ni-B, the presence of Ni causes B enrichment on the surface and also provides excess electrons to Co sites.

The ternary alloy Co-30Ni-B yields better HER activity than binary alloys of Co-B and Ni-B at various pH values. The result is attributed to the higher electron density at the Co sites of Co-30Ni-B. Current densities of 20 mA/cm^2 and 40 mA/cm^2 at overpotentials of 213 mV and 251 mV, respectively, are observed which are one of the best results obtained for any metal boride electrocatalyst in pH 7. In addition, we observed that the overpotential decreases from acidic to basic media with values of 209 mV, 170 mV, 83 mV, 60 mV and 45 mV (all vs RHE) for pH 1, 4.4, 7, 9.2 and 14 respectively signifying that Co-30Ni-B is capable of HER under different pH conditions especially in basic media. Finally, negligible loss in activity was observed for Co-

30Ni-B catalyst cycled over 1000 times in pH 7 and pH 14, making it an ideal material for industrial scale electrolysis.

Acknowledgement

The research activity is partially supported by UGC-UPE Green Technology Project, India and PAT (Provincia Autonoma di Trento) project ENAM in cooperation with Istituto PCB of CNR (Italy). A. Dashora is thankful to DST New Delhi, India for INSPIRE Faculty Project. R. Fernandes and N. Patel acknowledges UGC for providing financial support through Dr. D. S. Kothari postdoctoral fellowship program and Faculty recharge program respectively. We thank Ketan Bhotkar for SEM analysis.

Appendix A: Supplementary material

Detailed calculation method to obtain TOF value, table showing concentration of Co and Ni measured through XRF, SEM image, XPS spectra and surface elemental composition, EXAFS data, theoretical model, polarization curves, Electrochemical Activity comparison table and TOF values.

References:

1. A. Doner, F. Tezcan, G. Kardas, Int. J. Hydrogen Energy 38 (2013) 3881-3888.
2. M. C. Tavares, S. A. S. Machado, L. H. Mazo, Electrochim. Acta 46 (2001) 4359–4369.
3. I. M. Kodintsev, S. Trasatti, Electrochim. Acta 39 (1994) 1803-1808.
4. M. Wua, P. K. Shena, Z. Weib, S. Songa, M. Nie, J. Power Sources 166 (2007) 310–316.
5. T. W. Lin, C. J. Liu, J. Y. Lin, Appl. Catal. B: Environ. 134 (2013) 75-82.
6. J. D. Benck, T. R. Hellstern, J. Kibsgaard, P. Hakthranont, T. F. Jaramillo, ACS Catal. 4 (2014) 3957−3971.

7. Y. Sun, C. Liu, D. C. Grauer, J. Yano, J. R. Long, P. Yang, C. J. Chang, J. Am. Chem. Soc. 135 (2013) 17699−17702.
8. K. Wang, D. Xi, C. Zhou, Z. Shi, H. Xia, G. Liu, G. Qiao, J. Mater. Chem. A 3 (2015) 9415-9420.
9. M. Zou, J. Chen, L. Xiao, H. Zhu, T. Yang, M. Zhang, M. Du, J. Mater. Chem. A 3 (2015) 18090-18097.
10. P. Xiao, Y. Yan, X. Ge, Z. Liu, J. Y. Wang, X. Wang, Appl. Catal. B: Environ. 154 (2014) 232-237.
11. W. Cui, Q. Liu, Z. Xing, A. M. Asiri, K. A. Alamry, X. Sun, Appl. Catal. B: Environ. 164 (2015) 144-150.
12. J. F. Callejas, J. M. McEnaney, C. G. Read, J. C. Crompton, A. J. Biacchi, E. J. Popczun, T. R. Gordon, N. S. Lewis, R. E. Schaak, ACS Nano 8 (2014) 11101-11107.
13. Z. Huang, Z. Chen, Z. Chen, C. Lv, M. G. Humphrey, C. Zhang, Nano Energy 9 (2014) 373–382.
14. P. Los, A. Lasia, J. Electroanal. Chem. 333 (1992) 115-125.
15. E. Ndzebet, O. Savadogo, Int. J. Hydrogen Energy 19-8 (1994) 687-691.
16. J. J. Borodzilqski, A. Lasia, J. Appl. Electrochem. 24 (1994) 1267-1275.
17. H. Vrubel, X. Hu, Angew. Chem. Int. Ed. 51 (2012) 12703 –12706.
18. S. Gupta, N. Patel, A. Miotello, D. C. Kothari, J. Power Sources 279 (2015) 620-625.
19. P. Zhang, M. Wang, Y. Yang, T. Yao, H. Han, L. Sun, Nano Energy (2015) http://dx.doi.org/10.1016/j.nanoen.2015.11.020.
20. R. Fernandes, N. Patel, A. Miotello, M. Filippi, J. Mol. Catal. A: Chemical 298 (2009) 1–6.
21. B. Delley, J. Chem. Phys. 113 (2000) 7756-7764.
22. J. P. Perdew, K. Burke, M. Ernzerhof, Phys. Rev. Lett. 77 (1996) 3865-3868.
23. S. Sarkar, S. Sampath, Chem. Commun. 50 (2014) 7359—7362.
24. E. J. Popczun, C. G. Read, C. W. Roske, N. S. Lewis, R. E. Schaak, Angew. Chem. Int. Ed. 53 (2014) 5427 –5430.
25. N. N. Greenwoord, V. Parish, P. Thornton, Q. Rev. Chem. Soc. 20 (1966) 441-464.
26. Y. Okamoto, Y. Nitta, T. Imanaka, S. Teranishi, J. Chem. Soc. Faraday Trans. 1 75 (1979) 2027-2039.
27. C. G. Morales-Guio, L. A. Stern, X. Hu, Chem. Soc. Rev. 43 (2014) 6555—6569.
28. Y. C. Luo, Y. H. Liu, Y. Hung, X. Y. Liu, C. Y. Mou, Int. J. Hydrogen Energy 38 (2013) 7280-7290.
29. H. Kadomatsu, F. Ishii, H. Fujiwara, J. Phys. Soc. Japan 47 (1979) 1078-1085.
30. B. Shen, S. Wei, K. Fang, J. F. Deng, Appl. Phys. A 65 (1997) 295-299.
31. M. Zeng, Y. Li, J. Mater. Chem. A, 3 (2015) 14942–14962.
32. J. Tian, Q. Liu, A. M. Asiri, X. Sun, J. Am. Chem. Soc. 136 (2014) 7587–7590.
33. J. Tian, Q. Liu, Y. Liang, Z. Xing, A. M. Asiri, X. Sun, ACS Appl. Mater. Interfaces 6 (2014) 20579−20584.
34. Z. Peng, D. Jia, A. M. Al-Enizi, A. A. Elzatahry, G. Zheng, Adv. Energy Mater. 5 (2015) 1402031.
35. Z. Pu, Q. Liu, P. Jiang, A. M. Asiri, A. Y. Obaid, X. Sun, Chem. Mater. 26 (2014) 4326−4329.
36. H. W. Liang, S. Bruller, R. Dong, J. Zhang, X. Feng, K. Mullen, Nat. Comm. 6 (2015).
37. E. J. Popczun, C. G. Read, C. W. Roske, N. S. Lewis, R. E. Schaak, Angew. Chem. Int. Ed. 53 (2014) 5427 –5430.
38. S. Cobo, J. Heidkamp, P. A. Jacques, J. Fize, V. Fourmond, L. Guetaz, B. Jousselme, V. Ivanova, H. Dau, S. Palacin, M. Fontecave, V. Artero, Nat. Mater. 11 (2012) 802-807.

39. W.F. Chen, C.H. Wang, K. Sasaki, N. Marinkovic, W. Xu, J. T. Muckerman, Y. Zhu, R. R. Adzic, Energy Environ. Sci. 6 (2013) 943–951.
40. W.F. Chen, K. Sasaki, C. Ma, A. I. Frenkel, N. Marinkovic, J. T. Muckerman, Y. Zhu, R. R. Adzic, Angew. Chem. Int. Ed. 51 (2012) 6131-6135.
41. Z. Xing, Q. Liu, W. Xing, A. M. Asiri, X. Sun, ChemSusChem 8 (2015) 1850–1855.
42. H. Fei, Y. Yang, Z. Peng, G. Ruan, Q. Zhong, L. Li, E. L. G. Samuel, J. M. Tour, ACS Appl. Mater. Interfaces 7 (2015) 8083–8087.
43. T. N. Ye, L. B. Lv, M. Xu, B. Zhang, K. X. Wang, J. Su, X. H. Li, J. S. Chen, Nano Energy 15 (2015) 335–342.
44. Z. Huang, C. Lv, Z. Chen, Z. Chen, F. Tian, C. Zhang, Nano Energy 12 (2015) 666–674.

Figures:

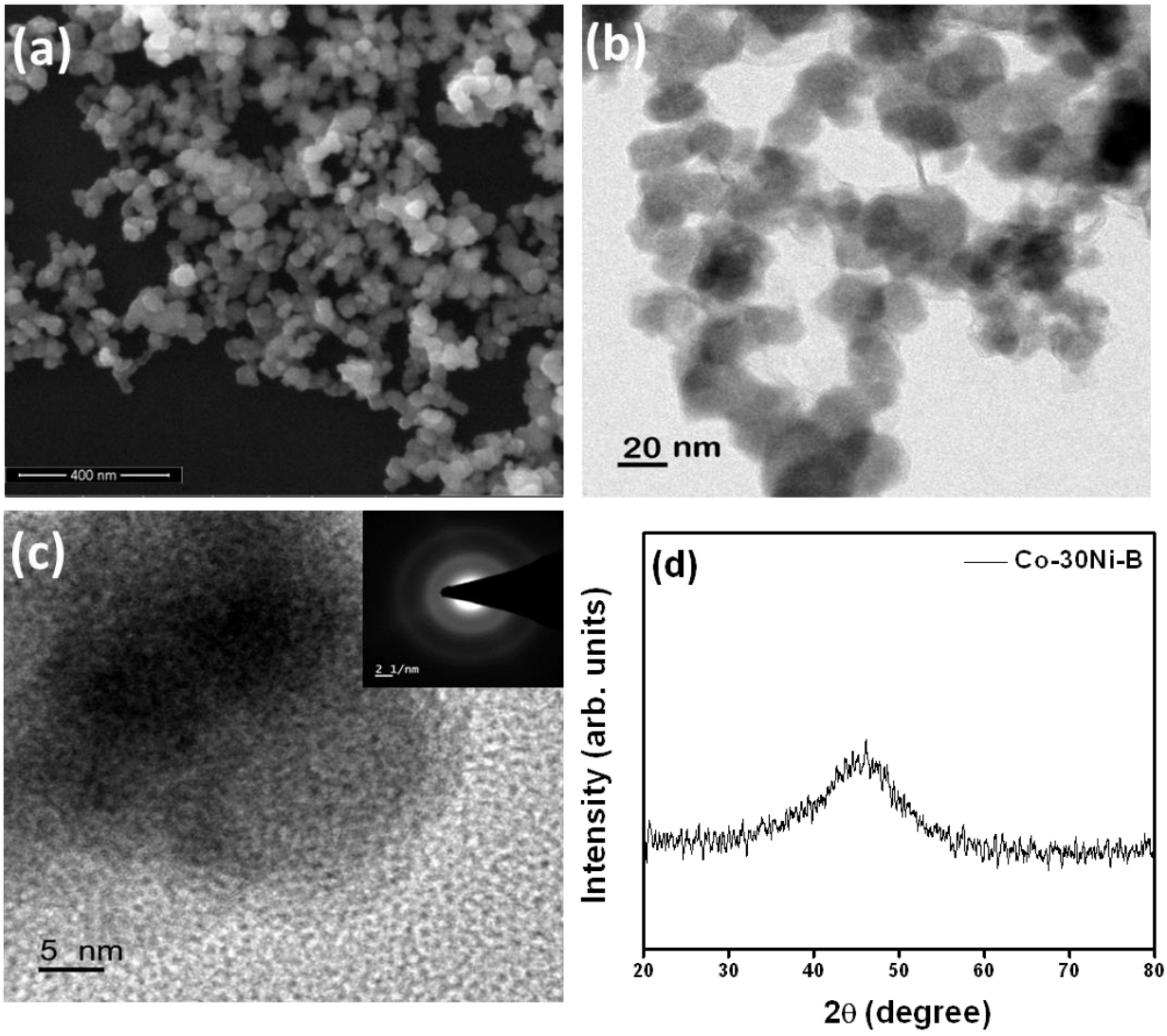

Fig. 1:(a) High resolution SEM image of Co-30Ni-B;**(b)**TEM image showing average size of Co-30Ni-B particles around 25 – 30 nm;**(c)** High resolution TEM image, SAED pattern**(inset of c)** and**(d)** XRD pattern showing presence of amorphous state in Co-30Ni-B.

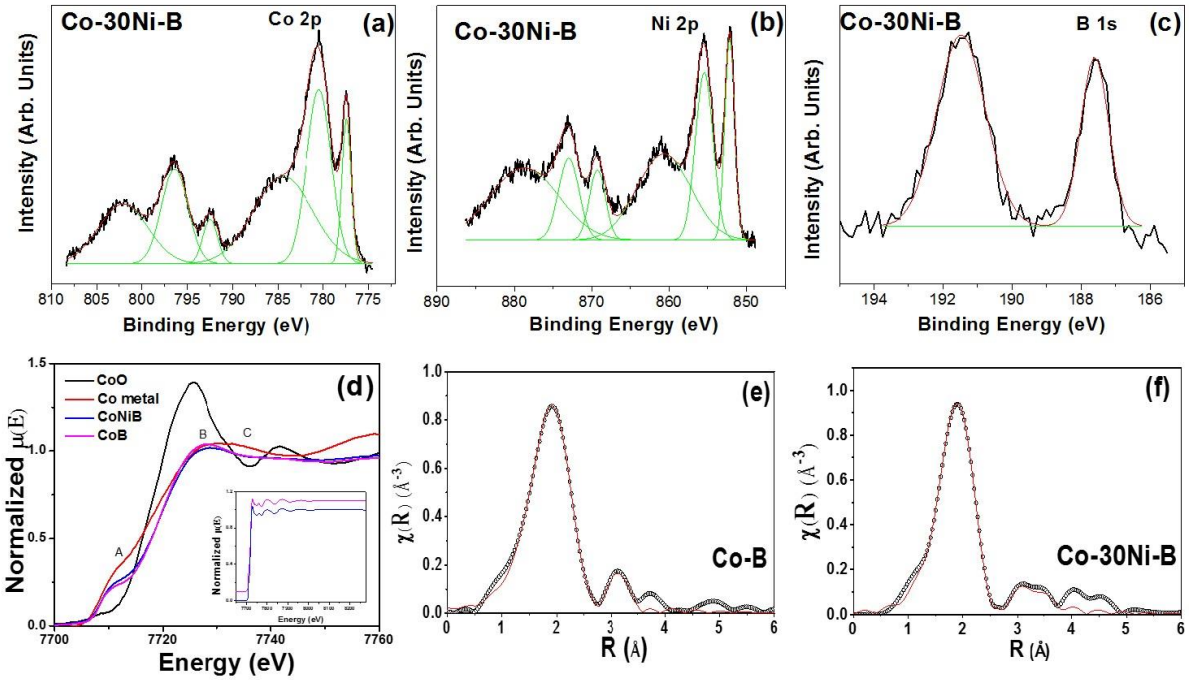

Fig. 2:XPS spectra of **Co 2p (a)**,**Ni 2p(b)** and **B 1s(c)** states; **(d)** XANES spectra of Co-30Ni-B is shown along with Co metal foil and CoO reference spectra and inset shows normalized EXAFS spectra of Co-B and Co-30Ni-B at Co K edge; Fourier transformed EXAFS spectra of **(e)** Co-B and **(f)**Co-30Ni-B measured at Co K edge (Scatter points) and theoretical fit (Solid line)

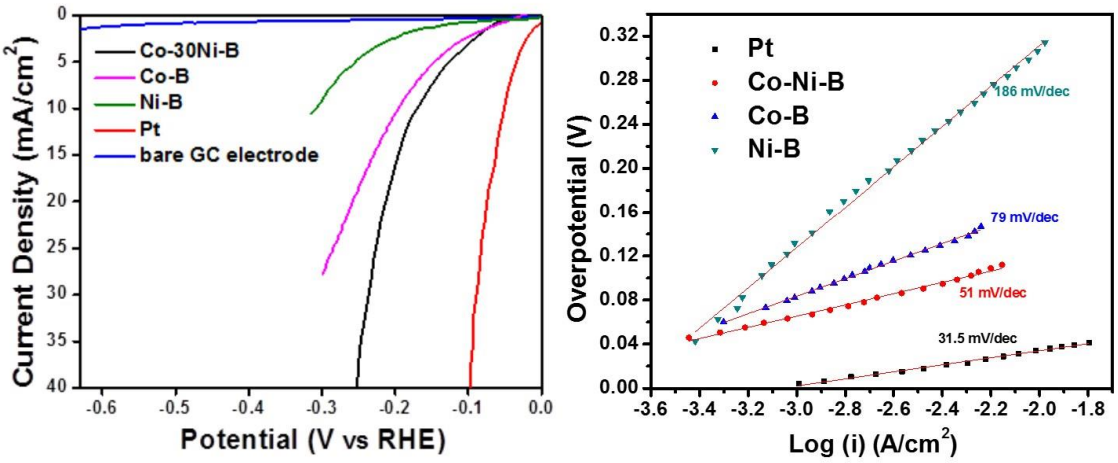

Fig. 3: (a) Linear polarization curves and **(b)** Tafel plots for Pt electrode, Co-30Ni-B, Co-B and Ni-B electrocatalysts in pH 7 at a scan rate of 5mV/s.

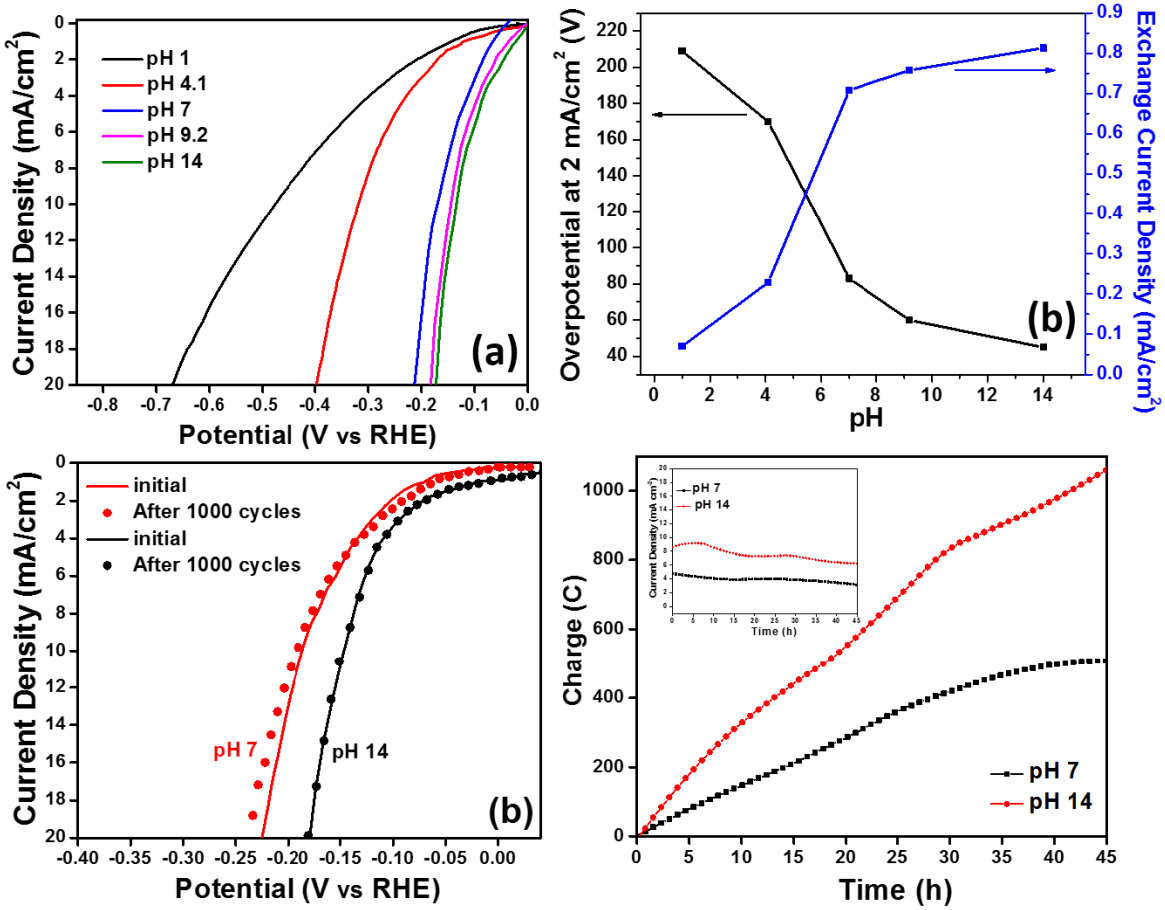

Fig. 4:(a) Linear polarization curves for Co-30Ni-B in different pH media (from pH 1 to pH 14); **(b)** Plot of overpotential (at 2 mA/cm2) and exchange current density values as a function of pH of the solution for Co-30Ni-B catalyst. **(c)** Linear polarization curves of Co-30Ni-B before and after 1000 cycles in 0.5 M KPi (pH 7) and 1 M NaOH (pH 14) (at a scan rate of 100 mV/s);**(d)** Plot of charge build-up versus time and time-dependent current density curves **(inset of d)** at constant overpotentials of 110 mV in pH 7 and 120 mV in pH 14.

Supporting Information

for

Co-Ni-B nanocatalyst for efficient hydrogen evolution reaction in wide pH range

S. Gupta[1], N. Patel[1, 2], R. Fernandes[1], R. Kadrekar[1], Alpa Dashora[3], A.K. Yadav[4],

D.Bhattacharyya[4], S.N. Jha[4], A. Miotello[2] and D.C. Kothari[1]

[1]Department of Physics and National Centre for Nanosciences & Nanotechnology, University of Mumbai, Vidyanagari, Santacruz (E), Mumbai 400098, India.

[2]Dipartimento di Fisica, Università degli Studi di Trento, I-38123 Povo (Trento), Italy.

[3]UM-DAE Centre for Excellence in Basic Sciences, Vidyanagari, Santacruz (E), Mumbai 400098, India.

[4]Atomic & Molecular Physics Division, Bhabha Atomic Research Centre, Mumbai – 400 085, India.

Experimental Method:

Reagents used:

Cobalt chloride hexahydrate [$CoCl_2.6H_2O$, 99%] (SDFCL), Nickel chloride hexahydrate [$NiCl_2.6H_2O$, 98%] (SDFCL), and sodium borohydride [$NaBH_4$, 98%] (SDFCL) were used for synthesizing the catalysts. Sodium hydroxide [NaOH, 98%] (Merck), di-potassium hydrogen orthophosphate [K_2HPO_4, 99%] (SDFCL), potassium dihydrogen orthophosphate [KH_2PO_4, 99.5%] (SDFCL), perchloric acid [$HClO_4$, 70%] (SDFCL) were used to prepare the electrolytic solutions. Double distilled water (DDW) was used for all practical purposes.

X-ray Absorption Spectroscopy (XAS) measurement details:

The EXAFS measurements were carried out at the Energy-Scanning EXAFS beamline (BL-9) (operating in energy range of 4 KeV to 25 KeV) at the INDUS-2 Synchrotron Source (2.5 GeV, 100 mA) at Raja Ramanna Centre for Advanced Technology (RRCAT), Indore, India [1]. Three ionization chambers (each of 300 mm length) were used for data collection in transmission mode, one ionization chamber for measuring incident flux (I_0), second one for measuring transmitted flux (I_t) and the third ionization chamber for measuring EXAFS spectrum of a reference metal foil (Mn foil in this case) for energy calibration. Appropriate gas pressure and gas mixture have been chosen to achieve 10-20% absorption in first ionization chamber and 70-90% absorption in second ionization chamber to improve the signal to noise ratio. Rejection of the higher harmonics content in the X-ray beam was performed by detuning the second crystal of a Si (111) (2d=6.2709) based double crystal monochromator (DCM). Powder samples of

appropriate weight, estimated to obtain a reasonable edge jump were taken in powder form and mixed thoroughly with cellulose powder to obtain total weight of 100 mg and homogenous pellets of 15 mm diameter were prepared using an electrically operated hydraulic press. The set of EXAFS data analysis available within IFEFFIT software package was used for EXAFS data analysis [2]. This includes background reduction and Fourier transform to derive the $\chi(R)$ versus *R* spectra from the absorption spectra (using ATHENA software), generation of the theoretical EXAFS spectra starting from an assumed crystallographic structure and finally fitting of experimental data with the theoretical spectra using ARTEMIS software.

Calculation of TOF values:

Molar mass of Co-30Ni-B = 128.5335 g/mol

Density = 8.04 g/cm^3

Molar volume = 15.9867 mL/mol

BET surface area: 168.2 cm^2/mg

Current densities in pH 7 for a catalyst loading of 2.1 mg/cm^2:

η_{50mV}: 0.35 mA/cm^2

η_{100mV}: 3.16 mA/cm^2

η_{150mV}: 7.63 mA/cm^2

η_{200mV}: 16.39 mA/cm^2

η_{250mV}: 38.46 mA/cm^2

Average surface atoms per 1 cm^2 of catalyst:

$$\left(\frac{3 * 6.022 * 10^{23}}{1\ mol} * \frac{1\ mol}{15.9867\ cm^3}\right)^{2/3} = 2.337 * 10^{15} atoms/cm^2$$

Surface atoms per testing area at 2.1 mg/cm^2:

$$\frac{2.1\ mg}{1\ cm^2\ (glassy\ carbon)} * \frac{168.2\ cm^2(catalyst)}{mg} * \frac{2.337 * 10^{15} atoms}{1\ cm^2(catalyst)} = 8.254 * 10^{17}\ \frac{atoms}{test\ area}$$

Turnover frequency (per surface atom) at overpotential of 250 mV:

$$\frac{1\ turnover}{2\ e^-} * \frac{38.46 * 10^{-3} A}{1\ cm^2} * \frac{1\ mol}{96485\ C} * \frac{6.022 * 10^{23} e^-}{1\ mol} * \frac{1\ test\ area}{8.254 * 10^{17} atoms} =$$

Catalyst	Concentration of Co and Ni (%)

0.145 $atom^{-1}\ s^{-1}$

Similar procedures were used for calculations of TOF values at different overpotentials and the values are represented in Figure S4 below.

	Co	Ni
Co-10Ni-B	89.0± 0.5	10.9± 0.2
Co-20Ni-B	80.1± 0.5	19.9± 0.2
Co-30Ni-B	70.9± 0.5	29.0± 0.3
Co-40Ni-B	59.9± 0.5	40.0± 0.3
Co-50Ni-B	48.6± 0.5	51.3± 0.3

Table S1. Percentage of Co and Ni content in different Co-Ni-B catalyst determined by X-ray fluorescence measurement.

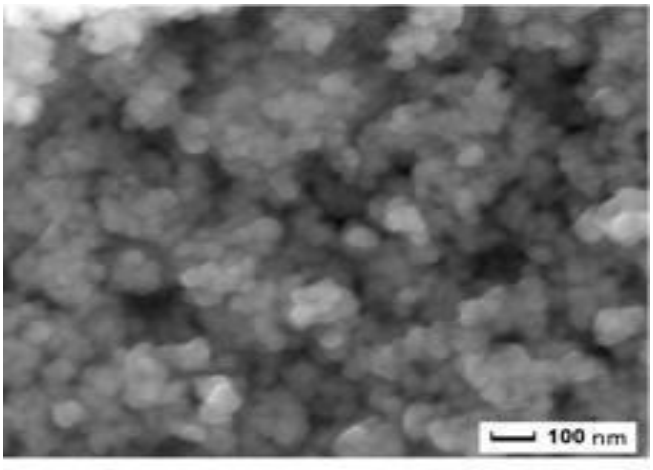

Figure S1: SEM image of Co-B catalyst powder

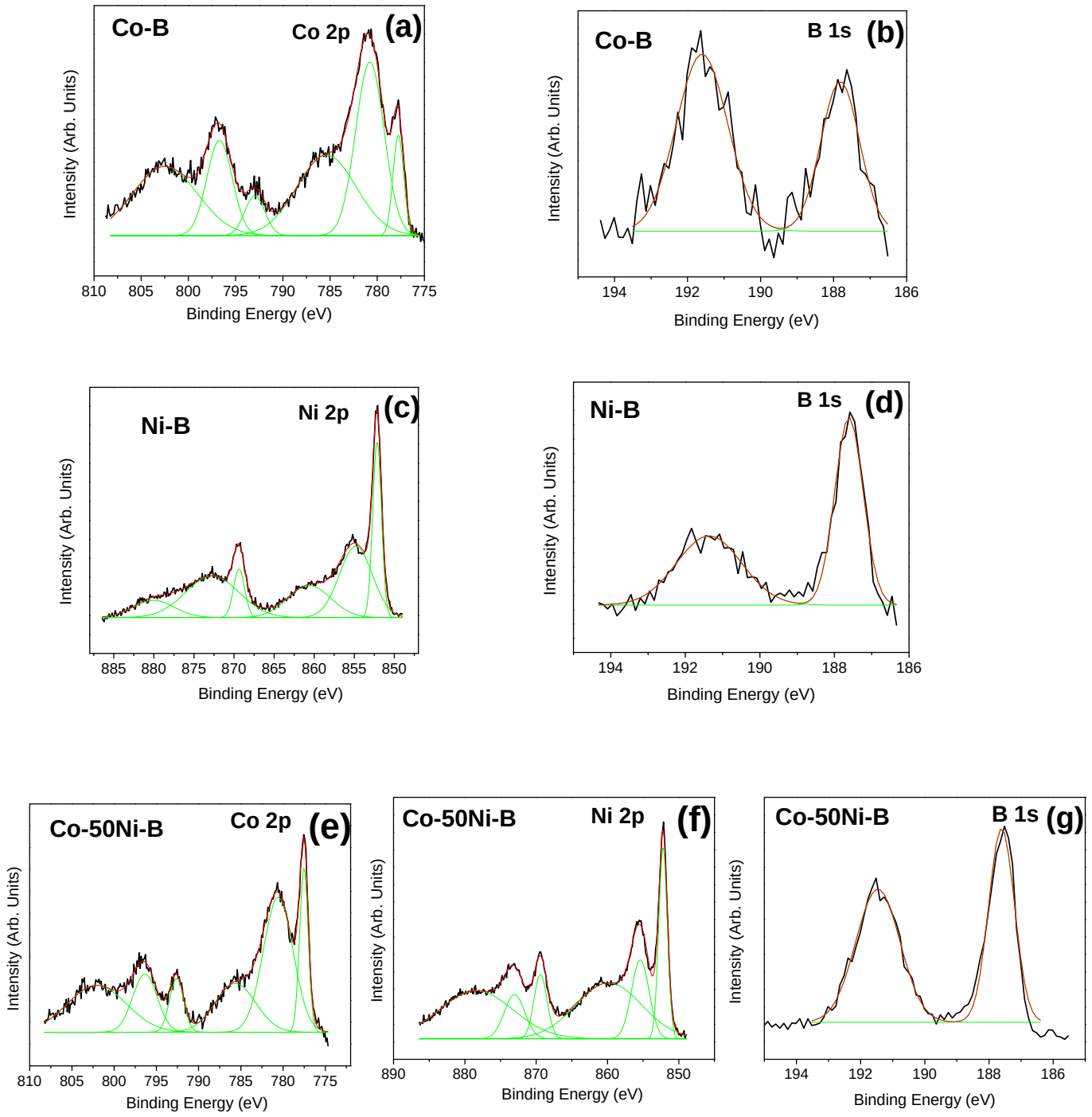

Fig. S2: XPS spectra of **Co 2p (a)** and **B 1s (b)** states in Co-B; **Ni 2p (c)** and **B 1s (d)** states in Ni-B;

Co 2p (e), **Ni 2p (f)** and **B 1s (g)** states in Co-50Ni-B electrocatalyst.

In Figure S2, X-ray photoelectron spectra (XPS) for Co $2p_{3/2}$ state shows presence of two peaks – 777.9, 780.7 eV for Co-B **(a)** and 777.5, 780.5 eV for Co-50Ni-B **(e)** where the low energy peak refers to elemental Co while the higher energy peak refers to oxidized Co. Similar BE peaks corresponding to elemental and oxidized states respectively were observed for Ni $2P_{3/2}$ levels – 852.2, 854.8 eV for Ni-B **(c)** and 852.2, 855.3 eV for Co-50Ni-B **(f)** and for B 1s levels –187.8, 191.6 eV for Co-B **(b)**, 187.6, 191.3 eV for Ni-B **(d)** and 187.6, 191.5 eV for Co-50Ni-B **(g)**.

In Co-B catalyst, the elemental boron peak is found to be positively shifted by about 0.8 eV as compared to the BE of pure B (187.0 eV). This shift indicates an electron transfer from the alloying B to the vacant d-orbital of the metallic Co, thus making the B atom electron deficient and the Co atom electron enriched. The absence of a chemical shift in the Co BE peak in the alloy catalyst is a result of the higher atomic number, and much higher concentration, of Co in relation to B. Ni-B and Co-50Ni-B catalysts show a similar increase in BE of elemental boron. However, in Co-50Ni-B, Co peak is negatively shifted by 0.5 eV as compared to metallic cobalt (777.9 eV) indicating higher electron density on cobalt sites.

Sample	**Peak Position (eV)**			**Concentration (%)**			
	Co	**Ni**	**B**	**Co**	**Ni**	**B**	**B/metal**

Co-B	**777.9**	**---**	**187.8**	**58**	**---**	**42**	**0.72**
Ni-B	**---**	**852.2**	**187.6**	**---**	**60**	**40**	**0.66**
Co-30Ni-B	**777.45**	**852.2**	**187.6**	**33**	**23**	**44**	**0.78**
Co-50Ni-B	**777.5**	**852.2**	**187.6**	**22**	**40**	**38**	**0.61**
Elemental peak	**778.5-777.9**	**852.9-852.3**	**186.4-187.0**				

Table S2. BE peak positions and percentage surface composition for all catalysts obtained from XPS analysis.

Table S3: Bond length, coordination number and disorder factor obtain by EXAFS fitting.

Paths	**Parameters**	**CoB**	**CoNiB**
Co-B	R (Å)	2.04	2.02
	N	4	4
	σ^2	0.0037	0.0058
Co-Co	R (Å)	2.48	2.43
	N	6	6
	σ^2	0.0095	0.0115
Co-B	R (Å)	3.34	3.29

	N	6	10
	σ^2	0.0132	0.0088
Co-Co	R (Å)	3.48	3.37
	N	6	3
	σ^2	0.0148	0.0120
Co-Ni	R (Å)		3.94
	N		3
	σ^2		0.0126

Figure S3: Nanoclusters of Co-B and Co-25Ni-B used for the calculation of charge transfer:

Nickel doped Co_2B nanoclusters

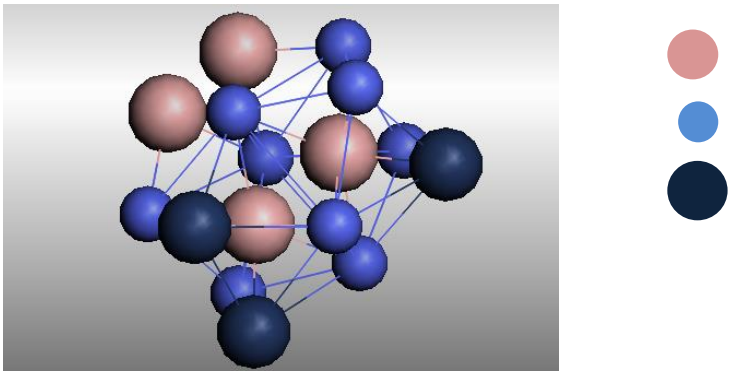

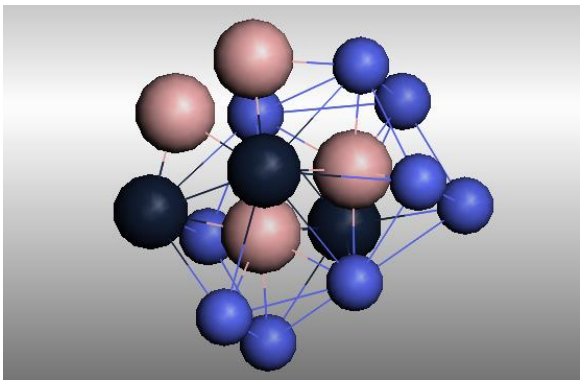

Pure Co_2B nanocluster

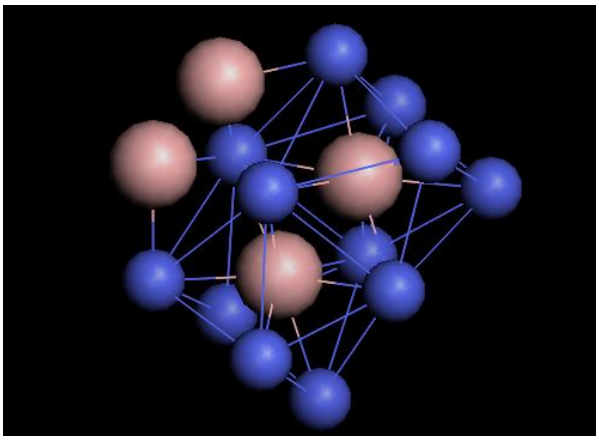

Catalyst	pH	Catalyst loading (mg/cm^2)	J_o (mA/cm^2)	Onset (mV)	Overpotential (mV)	Tafel slope (mV/dec)
Co-S film[3]	7	0.079	0.256	43	83 at 2 mA/cm^2	93
H_2-Cocat[4]	7	0.059	0.003	50	385 at 2 mA/cm^2	140
	7		-	45	65 at 2 mA/cm^2	93

					106 at 10 mA/cm^2	
Co-P/CC nanowire array[5]	0	0.92	0.288	38	67 at 10 mA/cm^2	51
	14		-	80	209 at 10 mA/cm^2	129
Cu2-Mo-S_4[6]	7	0.041	0.040	160	210 at 2 mA/cm^2	95
Co-P4-N_2[7]	7		-	80	230 at 2 mA/cm^2	-
Co-P/Ti[8]	7	2	-	100	102 at 2 mA/cm^2 149 at 10 mA/cm^2	58
	0		-	-	90 at 10 mA/cm^2	43
Fe-P/Ti[9]	7	-	-	100	200 at 10 mA/cm^2	99
	0	-	-	60	116 at 10 mA/cm^2	66
Fe-P/Ti[10]	6.5	~1	-	-	102 at 10 mA/cm^2 136 at 20 mA/cm^2	-
	0.3		0.43		50 at 10 mA/cm^2	37
Fe-P/CC[11]	7	4.1	-	46	60 at 2 mA/cm^2 115 at 10 mA/cm^2	70
	0		0.59	-	39 at 10 mA/cm^2	32
FeP nanorod array[12]	7	1.5	-	112	202 at 10 mA/cm^2	71
	0		0.5	20	58 at 10 mA/cm^2	45
	14		-	86	218 at 10 mA/cm^2	146
Mo-P NS on Carbon Flake[13]	7	~0.36	-	-	300 at 1 mA/cm^2	77.8
	0			100	200 at 10 mA/cm^2	56.4
WP_2nanorods[14]	7	0.5	-	-	172 at 2 mA/cm^2 298 at 10 mA/cm^2	79
	0		0.013	56	148 at 10 mA/cm^2	52
	14		-	-	225 at 10 mA/cm^2	84
W-P Nanoarrays on CC[15]	7	2	-	100	95 at 2 mA/cm^2 200 at 10 mA/cm^2	125
	0		0.29	50	130 at 10 mA/cm^2	69
	14		-	-	150 at 10 mA/cm^2	102
W_2N Nanoarrays on CC[16]	7	-	-	-	186 at 2 mA/cm^2 302 at 10 mA/cm^2	182
	0	-	-	-	198 at 10 mA/cm^2	92
	14	-	-	-	285 at 10 mA/cm^2	-
MoS2/N-graphene aerogel[17]	7	0.704			167 at 5 mA/cm^2 261 at 10 mA/cm^2	230
NiS2 nanosheets on CC[18]	7	4.1	-	150	193 at 2 mA/cm^2 243 at 10 mA/cm^2	69
	14		-	70	78 at 2 mA/cm^2 149 at 10 mA/cm^2	104
	7		0.893	39	72 at 10 mA/cm^2 130 at 50 mA/cm^2	67.8

$Ni_{0.33}Co_{0.67}S_2$ Nanowires[19]	0	0.3	-	65	73 at 10 mA/cm^2	44.1
	14		-	50	88 at 10 mA/cm^2	118
CoS_2 Nanowires[19]	7	0.3	0.976	52.5	87 at 10 mA/cm^2	87.1
	0				140 at 10 mA/cm^2	121
NiS_2 Nanoflakes[19]	7	0.3	0.643	77.6	187 at 10 mA/cm^2	105.1
	0				245 at 10 mA/cm^2	220
C coated Co_9S_8 NPs[20]	7	~0.28	-	-	150 at 1 mA/cm^2 280 at 10 mA/cm^2	-
	0		-	-	240 at 10 mA/cm^2	-
	14		-	-	250 at 10 mA/cm^2	-
Cu(0) catalyst[21]	7	-	-	70	157 at 1 mA/cm^2	127
Mo2C@NC[22]	7	~0.28	-	-	156 at 10 mA/cm^2	-
	0		0.096	-	124 at 10 mA/cm^2	60
	14			-	60 at 10 mA/cm^2	-
Mo2C in N-doped CNTs[23]	7	3	-	-	645 at 10 mA/cm^2	-
	0		-	-	147 at 10 mA/cm^2	71
	14		-	-	257 at 10 mA/cm^2	-
CoNx/C[24]	7	2	-	30	247 at 10 mA/cm^2	-
	0		-	20	133 at 10 mA/cm^2	57
	14		-	30	170 at 10 mA/cm^2	-
Ni-Bx films[25]	7		0.851	-	54 at 10 mA/cm^2	77
	0		0.380	-	45 at 10 mA/cm^2	43
	14		0.275	-	135 at 10 mA/cm^2	88
Co-B*	**7**	**~2.14**	**0.501**	**65**	**97 at 2 mA/cm^2**	**71**
	14				**166 at 10 mA/cm^2** **290 at 100 mA/cm^2**	
Co-30Ni-B*	**7**	**~2.14**	**0.708**	**53**	**83 at 2 mA/cm^2** **170 at 10 mA/cm^2** **251 at 40 mA/cm^2**	**51**
	1			**-**	**333 at 5 mA/cm^2** **479 at 10 mA/cm^2**	
	14			**-**	**93 at 5 mA/cm^2** **133 at 10 mA/cm^2** **233 at 100 mA/cm^2**	

*** This work**

Table S4: Comparison of electrochemical parameters for HER between Co-30Ni-B catalyst and various solid-state catalysts active in neutral and wide pH media.

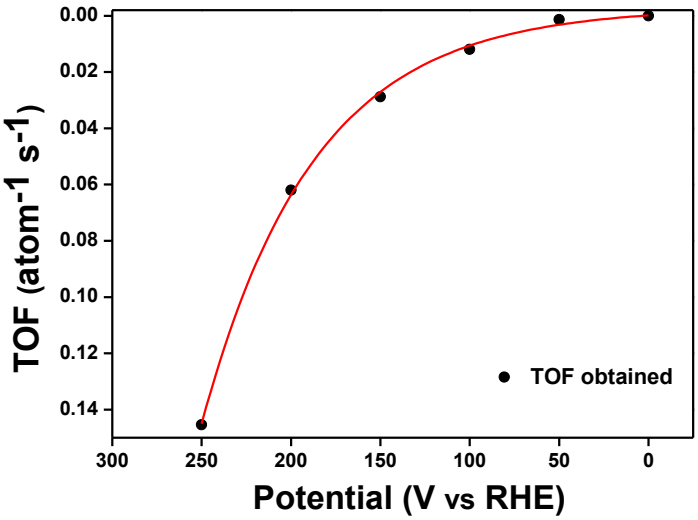

Figure S4: TOFs calculated for Co-30Ni-B catalyst as a function of overpotential (vs RHE) at pH 7.

Table S5: Comparison of TOF values with other reports from literature in pH 7.

Catalyst	Overpotential (V vs RHE)	TOF ($atom^{-1}$ s^{-2})
Co-30Ni-B	0.250	0.145
Co-B	0.250	0.072
Co-S film[3]	Not mentioned	0.017
H2-Cocat[4]	0.385	0.022
MoS_3-CV film[26]	0.340	0.300

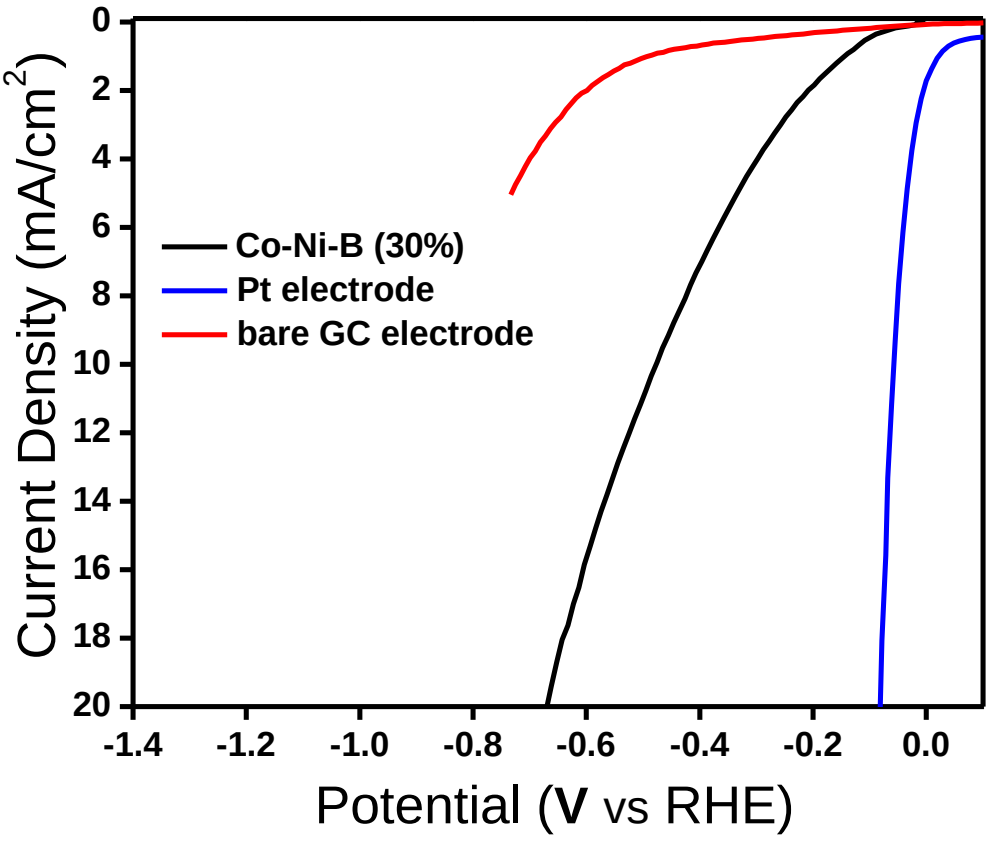

Figure S5: Polarization curves of Co-30Ni-B, Co-B, Pt electrode and bare glassy carbon electrode in 0.1 M $HClO_4$ solution (pH 1) solution obtained at a scan rate of 5 mV s^{-1}

Co-30Ni-B	Overpotential (mV)					
	1 mA	2 mA	5 mA	10 mA	20 mA	100 mA
pH 1	147	209	333	479		
pH 4.1	121	170	251	317		
pH 7	66	83	126	170	213	
pH 9.2	35	60	106	144	182	
pH14	21	45	93	133	172	233

Table S6. Table showing the current density values at various overpotentials for Co-30Ni-B catalyst in different pH solutions.

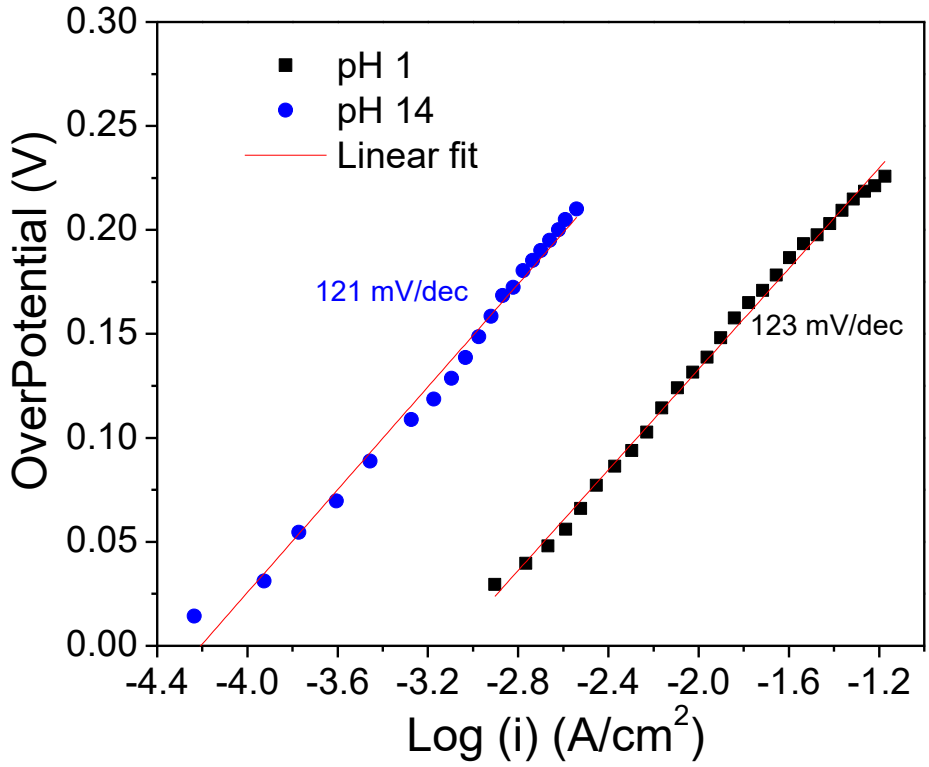

Figure S6: Tafel plot of Co-30Ni-B in pH 1 and pH 7

References:

1. S. Basu, C. Nayak, A. K. Yadav, A. Agrawal, A. K. Poswal, D. Bhattacharyya, S. N. Jha, N. K. Sahoo, India. J. Phys.: Conf. Ser. 493 (2014) 012032.
2. M. Newville, B. Ravel, D. Haskel, J. J. Rehr, E. A. Stern, Y. Yacoby, Physica B 208 (1995) 154-156.
3. Y. Sun, C. Liu, D. C. Grauer, J. Yano, J. R. Long, P. Yang, C. J. Chang, J. Am. Chem. Soc. 135 (2013) 17699−17702.

4. S. Cobo, J. Heidkamp, P. A. Jacques, J. Fize, V. Fourmond, L. Guetaz, B. Jousselme, V. Ivanova, H. Dau, S. Palacin, M. Fontecave, V. Artero, Nat. Mater. 11 (2012) 802-807.
5. J. Tian, Q. Liu, A. M. Asiri, X. Sun, J. Am. Chem. Soc. 136 (2014) 7587–7590.
6. P. D. Tran, M. Nguyen, S. S. Pramana, A. Bhattacharjee, S. Y. Chiam, J. Fize, M. J. Field, V. Artero, L. H. Wong, J. Loo, J. Barber, Energy Environ. Sci. 5 (2012) 8912-8916.
7. L. Chen, M. Wang, K. Han, P. Zhang, F. Gloaguen, L. Sun, Energy Environ. Sci. 7 (2014) 329–334.
8. Z. Pu, Q. Liu, P. Jiang, A. M. Asiri, A. Y. Obaid, X. Sun, Chem. Mater. 26 (2014) 4326−4329.
9. Z. Pu, C. Tang, Y. Luo, Int. J. Hydrogen Energy 40 (2015) 5092-5098.
10. J. F. Callejas, J. M. McEnaney, C. G. Read, J. C. Crompton, A. J. Biacchi, E. J. Popczun, T. R. Gordon, N. S. Lewis, R. E. Schaak, ACS Nano 8 (2014) 11101-11107.
11. J. Tian, Q. Liu, Y. Liang, Z. Xing, A. M. Asiri, X. Sun, ACS Appl. Mater. Interfaces 6 (2014) 20579−20584.
12. Y. Liang, Q. Liu, A. M. Asiri, X. Sun, Y. Luo, ACS Catal. 4 (2014) 4065−4069.
13. W. Cui, Q. Liu, Z. Xing, A. M. Asiri, K. A. Alamry, X. Sun, Appl. Catal. B: Environ. 164 (2015) 144–150.
14. H. Du, S. Gu, R. Liu, C. M. Li, J. Power Sources 278 (2015) 540-545.
15. Z. Pu, Q. Liu, A. M. Asiri, X. Sun, ACS Appl. Mater. Interfaces 6 (2014) 21874−21879.
16. J. Shi, Z. Pu, Q. Liu, A. M. Asiri, J. Hu, X. Sun, Electrochim. Acta 154 (2015) 345–351.
17. Y. Hou, B. Zhang, Z. Wen, S. Cui, X. Guo, Z. He, J. Chen, J. Mater. Chem. A 2 (2014) 13795-13800.
18. C. Tang, Z. Pu, Q. Liu, A. M. Asiri, X. Sun, Electrochim. Acta 153 (2015) 508–514.
19. Z. Peng, D. Jia, A. M. Al-Enizi, A. A. Elzatahry, G. Zheng, Adv. Energy Mater. 5 (2015) 1402031.
20. L. L. Feng, G. D. Li, Y. Liu, Y. Wu, H. Chen, Y. Wang, Y. C. Zou, D. Wang, X. Zou, ACS Appl. Mater. Interfaces 7 (2015) 980−988.
21. X. Liu, S. Cui, Z. Sun, P. Du, Chem. Commun. 51 (2015) 12954-12957.
22. Y. Liu, G. Yu, G. D. Li, Y. Sun, T. Asefa, W. Chen, X. Zou, Angew. Chem. Int. Ed. 54 (2015) 10752 – 10757.
23. K. Zhang, Y. Zhao, D. Fu, Y. Chen, J. Mater. Chem. A 3 (2015) 5783–5788.
24. H. W. Liang, S. Bruller, R. Dong, J. Zhang, X. Feng, K. Mullen, Nat. Comm. 6 (2015).
25. P. Zhang, M. Wang, Y. Yang, T. Yao, H. Han, L. Sun, Nano Energy (2015) http://dx.doi.org/10.1016/j.nanoen.2015.11.020.
26. D. Merki, H. Vrubel, L. Rovelli, S. Fierro, X. Hu, Chem. Sci. 3 (2012) 2515-2525.